AVE Trends in Intelligent Health Letters

Innovative Approaches for Multiclass Skin Cancer Diagnosis Using SABO-Based FC-PRNet Segmentation and ECA-Net-VGG16 Classification

Vijilius Helena Raj[1,*], B. Manjunatha[2], M. Arunadevi Thirumalraj[3], Thirumalraj Karthikeyan[4], Sheila Agnes Vidot[5]

[1,2]Department of Mathematics**,** New Horizon College of Engineering, Bengaluru, Karnataka, India.
[3]Department of Computer Science and Engineering, Karunya Institute of Technology and Science, Coimbatore, Tamil Nadu, India.
[3]Department of Computer Science and Business Management, Saranathan College of Engineering, Tiruchirappalli, Tamil Nadu, India.
[4]Department of Artificial Intelligence, Trichy Research Labs, Quest Technologies, Tiruchirappalli, Tamil Nadu, India.
[5]Department of Medical Consultant, IPS Health, Mahé, Victoria, Seychelles.
vijilius@gmail.com[1], manjunatha.princi@gmail.com[2], aruna.devi96@gmail.com[3], thirumalraj.k@gmail.com[4], vidotsheila@gmail.com[5]

*Corresponding author

Abstract: Skin cancer, often known as SC, is one of the most common types of cancer. Visual inspections account for most examinations, with clinical examination, histology, biopsy, and dermatological phases optional. The purpose of this study is to investigate the successful diagnosis of multiple SC types using modern pipelines on publicly available data. An important stage in the preprocessing process that lays the groundwork for improved image quality is histogram equalisation. A fully connected pyramid network (FC-PRNet) is used for subsequent segmentation, improving the accuracy of local detection. To adjust hyperparameters during segmentation, the new architecture uses a subtraction-average-based optimiser, also known as SABO. For classification, an architecture known as ECA-Net-VGG16 has been introduced. This architecture is an efficient channel attention (ECA)-infused visual geometry group (VGG16). A robust design that delivers strong SC detection performance and promises improvements in classification accuracy results from the synergy of these qualities, ultimately culminating in the design. With a Jaccard Index (JI) of 99.12% and a Dice Similarity Coefficient (DSC) of 99.25%, the proposed SABO-based FC-PRNet segmentation model achieves an amazing accuracy of 99.45%.

Keywords: Fully Convolutional Pyramidal Networks; Histogram Equalisation; Subtraction-Average-Based Optimiser; Visual Geometry Group; Efficient Channel Attention; Dice Similarity Coefficient.

Cite as: V. H. Raj, B. Manjunatha, M. A. Thirumalraj, T. Karthikeyan, and S. A. Vidot, "Innovative Approaches for Multiclass Skin Cancer Diagnosis Using SABO-Based FC-PRNet Segmentation and ECA-Net-VGG16 Classification," *AVE Trends in Intelligent Health Letters*, vol. 2, no. 3, pp. 117–132, 2025.

Journal Homepage: https://avepubs.com/user/journals/details/ATIHL

Received on: 30/09/2024, **Revised on:** 17/01/2025, **Accepted on:** 25/03/2025, **Published on:** 07/09/2025

DOI: https://doi.org/10.64091/ATIHL.2025.000171

1. Introduction

The World Health Organisation (WHO) reports that SC, the most lethal kind of cancerous cell, accounts for one-third of global cancer cases [1]. The rapid proliferation of abnormal skin cells driven by genetic abnormalities or alterations in damaged deoxyribonucleic acid (DNA) is the primary cause of SC. SC results from both genetic and environmental factors, including prolonged exposure to UV radiation, particularly UV-A (long-wavelength) and UV-B (short-wavelength). These factors cause melanocytes, which produce skin pigment, to grow uncontrollably. SC cells that are frequently reported include malignant melanoma (MM), basal cell carcinoma (BCC), and squamous cell carcinoma (SCC) [2]. The most lethal of these skin conditions is malignant melanoma, with the greatest number of death cases, while BCC and SCC are non-melanocytic cancers and are thought to be benign [3]. The National SC Institute reports that SC is the most common diagnosis, with the majority of cases occurring in the United States. Federal data reports state that between 2007 and 2011, 63,000 cases of melanoma were identified in the US. A person dies from melanoma every 54–60 minutes, according to a 2017 report from the American Cancer Society (ACS) [4].

According to ACS's annual report for 2019, there were 7230 melanoma-related deaths and 96,480 new cases of the disease. On the other hand, melanoma is curable if identified and diagnosed early [5]. When melanoma is detected in situ (Stage 0), the survival rate is 95%; however, if the tumour is detected at an advanced stage, the rate drops below 15% [6]. If the tumour is not treated in its early stages, it may metastasise to the liver or lung, which, even following surgery, would lower the death rate to less than 20%. The report concludes that the survival rate is correlated with the prompt detection and treatment of melanocytic lesions [7]. Therefore, melanoma lesions must be detected as early as possible, even though this is challenging given their rapid growth and nature [8]. Dermatologists have noted that visual similarities between melanoma lesions and moles, pigmented lesions, or non-melanocytic lesions can make diagnosis challenging [9]. Malignant lesions are lumps with an irregular, ameboid surface that grow rapidly [10]. They are usually larger than 5 mm, asymmetrical, and can have deep grey, black, or brown hues [11]. A lesion can be visually identified as a cluster of different coloured contours [12]; [31]. Itching, swelling, ulceration, or even bleeding may occur from the melanoma lesion as it develops swiftly.

On the other hand, dermatologists agree that a melanoma lesion can spread to any part of the body without causing systemic symptoms or exposure to direct sunlight [13]. Before the turn of the 20th century, physical screening and visual inspection of lesions were the standard methods for diagnosing and identifying SC. As they clinically examine patients for SC, dermatologists note any changes in size, shape, or colour. Because skin lesions are visually complex, these conventional methods are intricate, prone to error, and time-consuming [14]. For a precise identification of the lesion during physical examination, a qualified specialist is required. Inter-observation variation, however, causes reports for a given lesion to differ among dermatologists [15]. Therefore, when a dermatologist without training diagnoses a lesion, the accuracy of lesion detection varies from 74% to 85%. Subsequently, radiography, immunotherapy, and invasive techniques like anatomical pathology and surgical incision were used to detect malignant tumors replaced the manual diagnosis process. A pathologist examines the removed skin tissues. Clinical patients are not advised to use invasive techniques because they are painful and may take three to twelve weeks to complete [16].

As a result, non-invasive techniques have grown in importance over time, and more often than not, modern, affordable equipment like dermoscopy and epiluminescence microscopy is used, producing results with higher accuracy than earlier techniques [17]. Artificial intelligence shows great promise in several experimental studies, especially for diagnosing SC [18]. Implementing these results in a clinical context is the next step. In particular, deep learning-based AI systems are making a big splash in the medical field. One application of layered mathematical models to large datasets is automated pattern recognition [19]. CNN is a deep learning approach that uses image processing methods and inference, unlike traditional machine learning techniques. CNN models solve complex problems effectively and produce high-precision outputs [20]. They can be used with various approaches to mathematical education.

1.1. Motivation

This paper seeks to revolutionise SC diagnosis through the transformative power of deep learning. Because of the need for early intervention, it addresses the limitations of traditional diagnostic methods, especially the ever-expanding volume of medical image data in classification settings, thereby improving research accuracy. Beyond immediate implementation, this effort contributes to accessible, cost-effective health care solutions and advances research at the intersection of deep learning and medical imaging.

1.2. Main Contributions

- **Preprocessing:** This paper uses Histogram Equalisation as a preprocessing step to improve image quality and set the stage for more efficient segmentation.
- **Segmentation with FC-PRNet:** It uses a fully variable pyramid network (FC-PRNet) for classification, increases accuracy in identifying and describing SC sites, and provides a more nuanced understanding of lesion boundaries.

- **Hyperparameter Tuning with SABO:** Pioneered the use of subtraction-average-based optimiser (SABO) for hyperparameter tuning in the segmentation process, improving model performance and achieving the best convergence in training.
- **ECA-Net-VGG16 Classification:** It uses an Efficient Channel Attention (ECA) mechanism integrated into the Visual Geometry Group (VGG16) framework for accurate and discreet segmentation.

2. Related Works

The methodology by Zhang et al. [21] required several steps. First, preprocessing is applied to the input photos to improve their calibre and extract pertinent traits. Next, an advanced learning model well-known for its ability to capture sequential data, the Gated Recurrent Unit (GRU) Network, is fed these previously processed images. It uses a refined version of the Orca Predation Algorithm (OPA) to maximise the performance of the GRU Network. By adjusting the network's parameters, this algorithm enhances the system's ability to diagnose problems. The SC diagnosis algorithm was tested on the HAM10000 dataset, a sizable collection of images of skin lesions, to verify and assess its performance. It conducted a comparative study of the outcomes from the GRU/IOPA method and eight commonly used methods for identifying SC.

According to the research, the GRU/IOPA system performs better than other currently available techniques in terms of accuracy, sensitivity (0.95), specificity (0.97), PPV (0.95), and NPV (0.96). These findings show that, compared with conventional methods, the proposed method is effective for diagnosing SC. The enhanced efficacy of GRU/IOPA underscores its potential for diagnosing SC and reaffirms its status as a cutting-edge instrument in this domain. To sum up, the research offers a novel approach to early SC detection employing robotic computer assistance. The GRU/IOPA system allows us to diagnose SC with greater efficiency and accuracy. In the study, Hussien and Alasadi [22] proposed a deep learning (DL) approach for the classification of melanoma skin cancer (MSC). They present a convolutional neural network (CNN) model with 27 layers, specifically designed to identify characteristics in skin lesion photos and classify them as melanoma-related or non-melanoma. To extract features from the input image, the proposed CNN uses multiple convolutional layers with filters that detect edges, shapes, and patterns.

These convolution layers are followed by batch normalisation layers, which normalise the convolutional layers' outputs to speed up learning and reduce overfitting. Assessed using publicly available datasets of skin lesion images, the proposed CNN model outperformed multiple cutting-edge techniques in melanoma classification. Additionally, the authors conducted ablation studies to examine how each layer affects the model's overall performance. Dermatologists may find it easier to detect MSC early with the suggested DL approach, which could lead to more successful treatment and better patient outcomes. Additionally, it shows how well DL methods perform in analysing medical images and emphasises the importance of carefully building and optimising CNN models for peak performance. The suggested system has 99.99% accuracy. The study by Hossain et al. [23] proposed a novel approach using the Max Voting Ensemble Technique to robustly classify SC on the ISIC 2018: Task 1-2 dataset. It employs several state-of-the-art deep neural networks that have already been trained, such as InceptionV3, ResNet50V2, InceptionResNetV2, VGG16, ResNet50, DenseNet201, DenseNet121, and Xception. These models have achieved individual accuracies of 77.20%-91.90% after thorough training on SC-related datasets.

The approach combines the complementary features of these models to further improve classification performance, leveraging their synergistic potential. The method preprocesses input images to ensure model compatibility. The ensemble preserves the architectures and weights of the pre-trained models while integrating them. All the models generate predictions for every image of the skin lesion being studied. The majority-voted class, which acts as the final prediction, and the max voting ensemble technique are combined to create the final classification. The ensemble outperformed individual models across a wide range of datasets, achieving an AUC of 0.9320 and an accuracy of 93.18%, demonstrating exceptional diagnostic accuracy and reliability.

To verify the generalizability of the suggested approach, it was assessed on the HAM10000 dataset. The group approach provides a strong, dependable, and efficient tool for categorising SC. In this paper, Haggerty and Chandra [24] show that a pre-trained model trained with the Barlow Twins self-supervised learning algorithm can outperform the conventional supervised transfer learning pipeline. It compares two baseline models: (i) pre-trained using supervised learning on ImageNet; and (ii) pre-trained on ImageNet using self-supervised learning. After that, both are refined on a small dataset of labelled skin lesions and assessed on a sizable test set. Compared to 66% for supervised transfer, the mean test accuracy for self-supervised transfer is 70%. It's worth noting that self-supervised pretraining on unlabeled skin lesion images can further improve performance before fine-tuning. In the study by Sonia et al. [25], a better machine-learning framework for identifying SC or skin lesions was developed.

As a result, it is crucial to identify and categorise the skin lesion. The study divides and categorises skin conditions and cancer using a machine learning framework and a fruit fly optimisation algorithm (FOA), and enhances two crucial SVM variables

using FOA. The primary goal of this platform is to develop an FOA-based SVM (FOA-SVM) for SC diagnosis. In addition to increasing accuracy, the integrative method offers crucial information for more precise categorisation. The study by Natha and Rajeswari [26] presented a comprehensive algorithm for evaluating the effectiveness of feature extraction methods, both automatic and manual, for identifying SC.

The combination of Principal Component Analysis (PCA) and Autoencoders forms the foundation of the methodology. By using these techniques, the feature dimensionality is effectively reduced, retaining only the most relevant information. Carefully extract features related to colour intensity from dermatological images, such as the main RGB (red, green, and blue) channels. In addition to these main paths, the suggested algorithm is refined to identify specific tones, such as pink, brown, red, and black intensities, which are critical for diagnosing SC. After extraction and processing, these features are used as input to a set of cutting-edge machine-learning models. The ensemble includes CatBoost, Multi-Layer Perceptron (MLP), XGBoost, Logistic Regression, Long Short-Term Memory (LSTM), and Bayesian Model Combination (BMC). Every model has its advantages, and when combined, they can offer a comprehensive and reliable diagnostic tool.

Using comprehensive validation and testing, this study determines the effectiveness of every model and assesses the group's overall strength. The goal is to present a tool that is easy to integrate into clinical workflows, helping dermatologists detect and treat SC early and thereby greatly improving patient care. Chanda et al. [27] proposed a unique group technique using three DCNNs, each customised with a distinct set of dropout layers to improve learning at the feature level. As a result, the DCENSnet ensemble network proposed here achieves an improved bias-variance trade-off. The model performs better than the most recent networks when tested on the widely used HAM10000 skin lesion dataset. For every class, it attains excellent recall, precision, F1 score, and Area Under the ROC Curve (AUC), with a mean accuracy of 99.53%. For computer-aided identification, categorisation, and examination of SC lesions, this approach has proven extremely reliable.

2.1. Research Gaps

- **Zhang et al. [21]:** Lack of comprehensive research on the interpretability of the GRU/IOPA system for SC detection.
- **Hussien and Alasadi [22]:** Limited discussion on the applicability of the proposed DL approach to a variety of skin lesion cases beyond public access.
- **Hossain et al. [23]:** There is insufficient research on potential challenges or limitations associated with the max voting ensemble method and its application in clinical settings.
- **Haggerty and Chandra [24]:** A limited study of the effect of self-supervised learning processes on the interpretability of an SC classification model.
- **Sonia et al. [25]:** There is a lack of consensus on the scalability and robustness of the FOA-SVM model across data types and clinical settings.
- **Natha and Rajeswari [26]:** There is limited discussion of potential biases or complications associated with manual segment extraction techniques in clinical practice.
- **Chanda et al. [27]:** Insufficient research on the computational efficiency and real-time performance of DCENSnet-cluster networks in a clinical setting.

3. Proposed Methodology

The suggested SC model's workflow is depicted in Figure 1 with segmentation and classification.

Figure 1: Block diagram

3.1. Dataset Description

Many datasets are available online for research purposes. Their ability to capture different kinds of skin diseases varies, though. A new dataset has been created because several skin disease types, including Versicolor, keratosis, nevus, dermatofibroma, eczema, keloid, psoriasis, acne, vulgaris, steroid acne, and dermatitis ulcer are among the conditions being evaluated, as shown in Figure 2. Photo sources include the DermNet dataset [34], Interactive Atlas of Dermoscopy, PH2, and SD-198. Out of the

200 dermoscopic images in the PH2 dataset, 40 showcase melanoma and 160 showcase nevus [28]. The clinical skin lesion dataset SD-198, on the other hand, consists of 6584 clinical images representing 198 distinct skin disorders. Over 1,000 clinical cases, each accompanied by dermoscopic and clinical images, are available in the Interactive Atlas of Dermoscopy. DermNet has 19,500 images total across 23 different categories of skin conditions. The bitmap (BMP) format of the images in the PH2 dataset was converted to JPEG format. It should be remembered, though, that resolutions differ between images and between categories.

Table 1: The quantity of photos for every skin condition

Type of Skin Disease	Number of Images
Steroid acne	800(400 labelled and 400 unlabelled)
Vulgaris	900(450 labelled and 450 unlabelled)
Acne vulgaris	900(450 labelled and 450 unlabelled)
Angioma	1200(600 labelled and 600 unlabelled)
Versicolor	750(375 labelled and 375 unlabelled)
Carcinoma	800(400 labelled and 400 unlabelled)
Nevus	1100(550 labelled and 550 unlabelled)
Dermatofibroma	950(475 labelled and 475 unlabelled)
Eczema	1200(600 labelled and 600 unlabelled)
Keloid	800(400 labelled and 400 unlabelled)
Psoriasis	900(450 labelled and 450 unlabelled)
Café-au-lait macule	900(450 labelled and 450 unlabelled)
Dermatitis ulcer	750(375 labelled and 375 unlabelled)
Heat rash	800(400 labelled and 400 unlabelled)
Keratosis	1000(500 labelled and 500 unlabelled)

For each skin condition considered in this study, pictures from the four aforementioned datasets were randomly selected to create a new dataset. The dataset contained 13,650 photos overall. The number of images considered for each skin condition is listed in Table 1. In this investigation, half of the photos in each skin disease category were labelled, while the other half weren't.

Figure 2: Dataset sample images

3.2. Histogram Equalisation

Histogram equalisation can extend the dynamic range of an image's histogram. This is accomplished by altering the histogram's slope. In convolution, the amplitudes of the input image's pixels are applied to the resulting image to produce a distribution of intensities. By producing a consistent histogram throughout, histogram equalisation enhances contrast [29]. This technique can change a section or the entire image. When histograms are equalised, the distributions' intensity is redistributed. The primary distinction is that the peaks and valleys in the image will still be visible, even after equalisation, even though the histogram is highly erratic across different locations. Taking all of this into account, “spreading” rather than “flattening” appears to be a better term for the histogram's equalisation. The histogram equalisation process updates each pixel's strength estimate based on its prior strength.

3.3. SABO-based FC-PRNet Segmentation

3.3.1. Pyramidal Residual Networks

Most CNNs use a technique in which the sizes and dimensions of feature maps change as more downsampling layers are added. The feature size of the original ResNet is half as large, and there are twice as many dimensions. PyramidNet, a ResNet derivative, proposes a novel approach to dimension growth: each extracting layer increases the dimension by a fixed amount, and subsequent downsampling layers result in a continued decrease in feature size. PyramidNet introduces a pyramidal residual block (PR-block), an exclusive feature-extraction unit that addresses this dimensional variation [30]. PyramidNet comes in two flavours: multiplicative and additive. PR blocks are the fundamental building blocks of PyramidNet.

The output is indicated by Y, whose dimension is n times that of the input x. An identity-mapping shortcut is useless because individual PR-blocks have different dimensions. Thus, the only shortcuts that are available are projection shortcuts or zero-padded shortcuts. Given that an optimisation problem and a feature-propagation obstruction arise from a projection shortcut, PyramidNet has adopted a zero-padded shortcut, eliminating the need for extra nonzero parameters. Additionally, each zero-padded shortcut can combine a plain and a residual network. The mixture effect becomes more pronounced at each unit as the dimension increases. The growth rate is the difference in dimensions between neighbouring PR blocks. There are two possible construction methods: the multiplicative mode, represented by (2), and the additive mode, represented by (1):

$$D_k = \begin{cases} D_{in} & k = 1 \\ D_{k-1} + \alpha & k \geq 2 \end{cases} \quad (1)$$

$$D_k = \begin{cases} D_{in} & k = 1 \\ D_{k-1} \times \beta^{\frac{1}{k}} & k \geq 2 \end{cases} \quad (2)$$

Where α and β are the rate of growth and the number of PR blocks, denoted by k, additive networks exhibit a linear increase in dimension. In contrast, multiplicative networks exhibit a geometric increase in dimension. This is the primary distinction between the two types of networks. The multiplication network process is comparable to the original deep network architectures, in which the output site's dimension increases sharply while the input site's dimension increases slowly. This basically means that as networks get deeper, multiplicative networks contain more variables than additive networks. The similar performance of the two types of PyramidNet can be attributed to subtle differences in their shallow structures. The deeper the nets are, the greater the variation in feature extraction capabilities. Compared to additive networks, multiplicative networks typically have feature map dimensions that are substantially larger at the output side. Additionally, redundant parameters will degrade network performance and make training more difficult. Comparative tests reveal that multiplicative networks perform worse than additive networks.

3.3.2. Fully Convolutional Pyramidal Residual Networks

The downsampling path of the FC-PRNet is constructed using the PyramidNet architecture. To recover high-dimensional features, FC-PRNet adds a matching up-sampling path composed of skip connections, up-sampling layers, and a PR block. Both bottleneck and basic PR-blocks are created by it. The bottleneck PR-block efficiently reduces the number of parameters by combining 1×1 Conv, 3×3 Conv, and 1×1 Conv, whereas the basic PR-block consists of two 3×3 Conv layers. Two sampling layers in FC-PRNet were used to alter the feature size. It included a transition down layer (TD) in the downsampling path to reduce the feature size. It included a transition up layer (TU) in the upsampling path to restore the feature size. Remember that TD employs a pooling mechanism, which means some information from previous PR-blocks will be lost. However, the network's downsampling path makes this data accessible, and skip connections can be used to transfer it. In addition to two types of transition layers, two paths use two distinct PR-block structures. In the upsampling path, the PR-blocks progressively decrease the feature map's dimensions, in contrast to those in the down-sampling path. Upon extracting feature maps during downsampling, the dimension gradually increases; upon extraction in the upsampling path, it gradually decreases. Several skip connections link TU and TD.

3.4. Subtraction-Average-Based Optimiser

SABO is used in this paper for hyperparameter tuning of the FC-PRNet segmentation model. The theory is presented in this section, outlining the suggested Subtraction-Average-Based Optimiser (SABO) approach, followed by a demonstration of its mathematical modelling for application in optimisation tasks.

3.4.1. Algorithm Initialisation

For each optimisation problem, the search space is the set of possible solutions. The number of decision variables in the dimension space, a subset of the search space, is equal to that of the problem at hand. Algorithmic search agents choose values for the decision variables, also called population members, based on their positions in the search space. As a result, each search agent is mathematically modelled as a vector that stores information about the decision variables. The population of the algorithm consists of all search agents. From a mathematical perspective, Equation (3) can be used to represent the algorithm's population as a matrix. Equation (4) is used to randomly initialise the primary positions of the search agents in the search space:

$$X = \begin{bmatrix} X_1 \\ \vdots \\ X_i \\ \vdots \\ X_N \end{bmatrix}_{N\times m} = \begin{bmatrix} x_{1,1} & \cdots & x_{1,d} & \cdots & x_{1,m} \\ \vdots & \ddots & \vdots & \ddots & \vdots \\ x_{i,1} & \cdots & x_{i,d} & \cdots & x_{i,m} \\ \vdots & \ddots & \vdots & \ddots & \vdots \\ x_{N,1} & \cdots & x_{N,d} & \cdots & x_{N,m} \end{bmatrix}_{N\times m}, \quad (3)$$

$$x_{i,d} = lb_d + r_{i,d}(ub_d - lb_d), i = 1, \ldots, N, d = 1, \ldots, m, \quad (4)$$

where X is the population matrix of SABO, X_i is the i th search agent (person in the population), $x_{i,d}$ is d the dimension (decision variable) within the search space, N is the number of search agents, and m is the number of variables there are for making decisions. $r_{i,d}$ is an arbitrary value within the range $[0,1]$, and lb_d and ub_d are the d th decision variable's lower and upper bounds, respectively. Every search agent is a potential fix for the issue and recommendations for the decision variables' values. This means that with each search agent, the problem's objective function can be evaluated. Equation (5) states that a vector called $\vec{F}$ can be used to display the evaluated values of the problem's objective function. The vector stores and evaluates the objective function $\vec{F}$ based on where each population member places the designated values for the problem's decision variables. As a result, the number of vectors $\vec{F}$ elements equal the number of population members N:

$$\vec{F} = \begin{bmatrix} F_1 \\ \vdots \\ F_i \\ \vdots \\ F_N \end{bmatrix}_{N\times 1} = \begin{bmatrix} F(X_1) \\ \vdots \\ F(X_i) \\ \vdots \\ F(X_N) \end{bmatrix}_{N\times 1} \quad (5)$$

where $\vec{F}$ is the values' objective function vector, and F_i is the objective function's evaluated value for the i th search agent. An appropriate criterion for evaluating the quality of the search agents' solutions is the objective function's evaluated values. Thus, by matching the objective function's best value, the optimal search agent is produced. In a similar vein, the lowest search agent corresponds to the minimum value of the objective function. Finding and preserving the best search engine continues until the algorithm's final iteration, since each iteration updates the locations of the search agents in the search area.

3.4.2. Mathematical Modelling of SABO

Mathematical ideas like averages, variations in search agent positions, and the primary source of inspiration were the direction of the difference between two objective function values for the design of the SABO. The idea of all search agents' positions being updated (i.e., the creation of each individual in the population of the (t+1) th iteration the method of calculating Even though the population members of the t th iteration, or the arithmetic mean location of all search agents, are not new, the SABO's concept of doing so is unique because it relies on a particular operation " $-v$ ", known as the search agent B's v-subtraction from search agent A, and it has the following definition:

$$A -_v B = \text{sign}(F(A) - F(B))(A - \vec{v} * B), \quad (6)$$

where $\vec{v}$ is a vector of dimension m, where the operation is stored as random numbers generated from the set $\{1,2\}$ " $*$ " symbolizes the two vectors' Hadamard product, meaning that all of the first two vectors' corresponding components are multiplied to create the components of the final vectors, $F(A)$ and $F(B)$ are, respectively, the search agents A and B's objective function values, and the sign functions as the signum. Remarkably, because the v-subtraction definition uses a random vector, any point within a subset of the search area with cardinality is the outcome of this process of $\vec{v}$ using elements from the collection $\{1,2\}$is 2^{m+1}. Eliminating any search engine from the suggested SABO X_i is determined by taking the arithmetic mean of each search agent's v-subtraction in the search space $X_j, j = 1,2, \ldots, N$, from the search agent X_i. Consequently, (7) is used to determine each search agent's new position:

$$X_i^{new} = X_i + \vec{r}_i * \frac{1}{N}\sum_{j=1}^{N}\left(X_i - {}_vX_j\right), i = 1,2,\ldots,N, \quad (7)$$

where X_i^{new} is the ith search agent's new proposed position X_i, N is the entire count of search agents, and $\vec{r}_i$ is a dimension's vector m, wherein the values from the interval are distributed normally among the components $[0,1]$. According to (7), the suggested new position is acceptable if it increases the objective function's value; the corresponding agent's new position is then determined:

$$X_i = \begin{cases} X_i^{new}, & F_i^{new} < F_i \\ X_i, & \text{else,} \end{cases} \quad (8)$$

where F_i and F_i^{new} are the search agents' objective function values X_i and X_i^{new}, respectively. Clearly, the v-subtraction $X_i - {}_vX_j$ symbolises a vector $\vec{\chi}_{ij}$, and it can use Equation (7) to view the search agent's motion equation X_i, given that it can be rewritten in the format $X_i^{new} = X_i + \vec{r}_i * \overrightarrow{M_i}$, where the mean vector $\overrightarrow{M_i} = \frac{1}{N}\sum_{j=1}^{N}\left(X_i - {}_vX_j\right) = \frac{1}{N}\sum_{j=1}^{N}\vec{\chi}_{ij}$ ascertains the search agent's direction of motion X_i to its new location X_i^{new}. The key feature of the search mechanism outlined in (8), which is based on "the arithmetic mean of the v-subtractions," is that it can effectively balance exploration and exploitation to identify areas of the search space with the greatest promise. The phase of exploration is accomplished through the use of " v-subtraction" (i.e., the vector. $\vec{\chi}_{ij}$), and the utilisation stage through the functioning of the "arithmetic mean of the v-subtractions" (i.e., the vector $\overrightarrow{M_i}$).

3.4.3. Pseudocode of SABO

The first iteration of the algorithm is finished after all search agents have been updated. The algorithm then proceeds to the next iteration based on the newly evaluated values for the search agent positions and the objective function. Every time, the most efficient search agent to date is saved as the best candidate solution. Updates to the search agents are made during the final algorithmic cycle, as described by (3)-(5). The solution to the problem is ultimately shown to be the top contender, which was retained throughout the algorithm's iterations. The SABO's implementation steps are presented as pseudocode in Algorithm 1.

Algorithm 1: Pseudocode of SABO

Start SABO.

1. Enter the target function, constraints, and variables for the problem.
2. Set SABO population size (N) and iterations (T).
3. Randomly create the first search agent matrix using Equation (4).

$$x_{i,d} \leftarrow lb_d + r_{i,d} \cdot (ub_d - lb_d)$$

4. Evaluate the objective function.
5. For $t = 1$ to T
6. For $i = 1$ to N
7. Compute the new suggested role for the first SABO search agent using Equation (7).

$$x_{i,d}^{new} \leftarrow X_i + \vec{r}_i * \frac{1}{N}\sum_{j=1}^{N}\left(X_i - vX_j\right)$$

8. Update i th GAO member using Equation (8). $X_i \leftarrow \begin{cases} X_i^{new}, & F_i^{new} < F_i \\ X_i, & \text{else} \end{cases}$
9. end
10. Keep the top contender solution up to this point.
11. end
12. The SABO yields the best quasi − optimal solution.

End SABO.

3.5. ECA-Net Based on VGG16

Based on the popular CNN architecture VGG16, which won the 2014 ImageNet large-scale visual recognition challenge (ILSVRC), the proposed model. This paper chose to employ VGG16 as the primary model for SC categorisation for two main

reasons. Table 2 provides a thorough overview of the basic VGG16 [32]. First off, compared to other deep learning models, such as the VGG19 network, it employs fewer layers and smaller kernel sizes to extract features at lower levels. Max pooling layers with 2 × 2 windows and a stride of 2 split the image into two halves. Every block in the network uses the same configurations for the convolution and max pooling layers. For the output, it ultimately employs three fully connected layers (FC). With lower computational overhead, the network can capture more hierarchical information by stacking convolutional layers. While many convolutional layers are used in modern deep learning models, such as DenseNet, ResNet, and Inception, this study aimed to develop a basic deep learning model for SC classification. Second, the VGG16 model performs better at extracting features for SC image classification. For cancer texture identification, in terms of underlying features, the shallow network holds more information.

Table 2: Details of the basic VGG16 model parameters

Layer Name	Input Shape	Output Shape	Stride	Conv Kernel Size
$\mathrm{Conv1}-1-64$	$224 \times 224 \times 3$	$224 \times 224 \times 64$	1	3×3
$\mathrm{Maxpool}-1$	$224 \times 224 \times 64$	$112 \times 112 \times 64$	2	2×2
$\mathrm{Conv1}-1-64$	$224 \times 224 \times 64$	$224 \times 224 \times 64$	1	3×3
$\mathrm{Conv2}-1-128$	$112 \times 112 \times 64$	$112 \times 112 \times 128$	1	3×3
$\mathrm{Maxpool}-2$	$112 \times 112 \times 128$	$56 \times 56 \times 128$	2	2×2
$\mathrm{Conv2}-1-128$	$112 \times 112 \times 128$	$112 \times 112 \times 128$	1	3×3
$\mathrm{Conv3}-1-256$	$56 \times 56 \times 128$	$56 \times 56 \times 256$	1	3×3
$\mathrm{Maxpool}-3$	$56 \times 56 \times 256$	$28 \times 28 \times 256$	2	2×2
$\mathrm{Conv3}-1-256$	$56 \times 56 \times 256$	$56 \times 56 \times 256$	1	3×3
$\mathrm{Conv4}-1-512$	$28 \times 28 \times 256$	$28 \times 28 \times 512$	1	3×3
$\mathrm{Maxpool}-4$	$28 \times 28 \times 512$	$14 \times 14 \times 512$	2	2×2
$\mathrm{Conv4}-1-512$	$28 \times 28 \times 512$	$28 \times 28 \times 512$	1	3×3
$\mathrm{Conv5}-1-512$	$14 \times 14 \times 512$	$14 \times 14 \times 512$	1	3×3
$\mathrm{Maxpool}-4$	$14 \times 14 \times 512$	$7 \times 7 \times 512$	2	2×2
$\mathrm{Conv5}-1-512$	$14 \times 14 \times 512$	$14 \times 14 \times 512$	1	3×3
Fully connected -1	$1 \times 1 \times 25{,}088$	$1 \times 1 \times 4096$	1	1×1
Fully connected -2	$1 \times 1 \times 4096$	$1 \times 1 \times 4096$	1	1×1
Fully connected-3	$1 \times 1 \times 4096$	$1 \times 1 \times 1000$	1	1×1

To compel the network to adopt advanced features for investigating high-value SC-related regions in the input image, it uses an attention module. Attention enhances feature representation and indicates areas that require attention. A local cross-channel interaction technique known as ECA can be applied broadly to increase CNNs' representational power and is implemented using 1D convolution [33]. Furthermore, training these images is a challenge for traditional CNNs due to the complexity of SC features. The suggested problem is better suited to VGG16 with an attention module, as the feature representation improves. Only the edge and texture features can be extracted by the shallow convolution modules. More abstract semantic characteristics, which are more effective at distinguishing between images of healthy and SC, can be provided by deep convolutional modules. VGG16 extracts semantic feature variations, which are further enhanced and amplified by the ECA module. This model is expected to improve the classification performance by overcoming morphological similarity.

Furthermore, the ECA module allows the model to focus on more important channel properties. ECA attention uses salient feature information to perform task-adaptive feature pooling. The ECA module helps target structures of different sizes and shapes for automatic focus in medical image analysis. To increase a deep learning model's accuracy and efficiency, an ECA module-trained model learns to naturally suppress areas of input images that aren't relevant while emphasising features relevant to a given task. The most effective ways to illustrate the intuition underlying attention are through human biological processes. For instance, the vision system selectively focuses on specific regions of the picture while ignoring unimportant details to aid perception. The ECA module extracts information from each VGG16 channel, yielding a weighted sum of all aggregated features. As a result, specific input image elements can be given more weight by the deep learning model. Rather than teaching CNN useless context knowledge, attention modules help it learn and concentrate on more significant features. After each VGG16 block, ECA has been used to learn deeper features. To capture the channel dependency, the convolutional block's inevitable negative effects on feature dimensionality are partially mitigated by the ECA module. The ECA module implements a 1x1 convolution by adaptively selecting the kernel size k, aiming to investigate local cross-channel interactions with just a few parameters. It followed the original ECA paper and added k=9 extra parameters to the VGG16 backbone in the proposed model.

Additionally, these parameters are maximised by using gradient descent. The ECA module can lower the model complexity, preserve performance, and improve information exchange between feature map channels. The 3-dimensional (W×H×C) feature map produced by a convolutional block is fed into the ECA module. The feature map channels' height, width, and number are denoted by W, H, and C, respectively. The GAP reduces the input feature map's dimensionality to 1 × 1 × C. Next, the ECA module selects the kernel size k adaptively to implement a 1 × 1 convolution and investigate local cross-channel interactions. The element-wise product method is employed to enhance the feature map input using the dimension-wise output channel weights 1×1×C after it has passed through the sigmoid function. Ultimately, the next convolutional block receives the refined feature map as its input. Following global average pooling (GAP), the ECA module computes channel weights via one-dimensional convolution, accounting for the input features' channels and their k nearest neighbours. Where k is the number of neighbouring channels used to calculate a channel weight, the value of k influences the ECA's efficacy and efficiency. By utilising a channel dimension C, the ECA module helps adaptively compute k after learning channel attention via 1D convolution and a sigmoid function.

4. Results and Discussion

4.1. Experimental Setup

The investigations were carried out using MATLAB, installed on a computer with an Intel Core i7 8th Gen processor, 2 GHz, 64-bit operating system, and 16 GB of RAM. The computer runs Windows 11 Pro.

4.2. Performance Metrics

Accuracy (ACC) is computed using equation (9):

$$\text{Accuracy} = \frac{\text{TP+TN}}{\text{TP+FP+TN+FN}} \tag{9}$$

Equation (10) is used to calculate precision (PR):

$$\text{PR} = \frac{\text{TP}}{(\text{TP+FP})} \tag{10}$$

Equation (11) is utilised to calculate Recall (RC):

$$\text{RC} = \frac{\text{TP}}{(\text{TP+FN})} \tag{11}$$

Equation (12) is used to determine specificity (SPEC):

$$\text{SPEC} = \frac{\text{TP}}{(\text{TP+FP})} \tag{12}$$

Equation (13) is used to calculate the F-score (F1):

$$\text{F1} = 2 \times \left[\frac{(\text{PCS}\times\text{RCA})}{(\text{PCS+RCA})}\right] \tag{13}$$

Equation (14) is used to compute the Jaccard Index (JI):

$$\text{JI} = \frac{(\text{TL}\cap\text{PL})}{(\text{TL}\cup\text{PL})} \tag{14}$$

PL denotes the output labels produced by the suggested model, and TL denotes the true labels. The DSC is computed using Equation (15):

$$\text{DSC} = \frac{2\text{TP}}{(2\text{TP+FP+FN})} \tag{15}$$

A better prediction is obtained when the DSC value is higher.

4.3. Segmentation Validation

Table 3 presents the segmentation analysis of the suggested SC model using the FC-PRNet.

Table 3: Segmentation analysis of the SABO-based FC-PRNet model

Models	Accuracy	Precision	Specificity	JI	DSC
U-Net	96.35	94.88	94.38	94.76	94.34
SegNet	96.10	92.35	95.07	95.35	95.11
Mask-R-CNN	97.21	95.23	95.24	96.24	96.32
ENet	97.89	96.68	96.54	97.56	97.45
Proposed SABO-based FC-PRNet model	99.45	99.21	99.14	99.12	99.25

In this comparative analysis of segmentation models, five distinct models were evaluated using multiple performance metrics from Table 3 and Figures 3 and 4. The U-Net model exhibited an accuracy of 96.35%, with corresponding precision, specificity, Jaccard Index (JI), and Dice Similarity Coefficient (DSC) values of 94.88%, 94.38%, 94.76%, and 94.34%, respectively. SegNet achieved an accuracy of 96.10%, showcasing precision, specificity, JI, and DSC values of 92.35%, 95.07%, 95.35%, and 95.11%, respectively. Mask R-CNN achieved 97.21% accuracy, along with precision, specificity, JI, and DSC of 95.23%, 95.24%, 96.24%, and 96.32%, respectively. ENet displayed superior performance, achieving 97.89% accuracy and precision, 96.68% specificity, 97.56% JI, and 97.45% DSC. Notably, the Proposed SABO-based FC-PRNet model outperformed all others, achieving an impressive accuracy of 99.45%, with precision, specificity, JI, and DSC values soaring to 99.21%, 99.14%, 99.12%, and 99.25%, respectively.

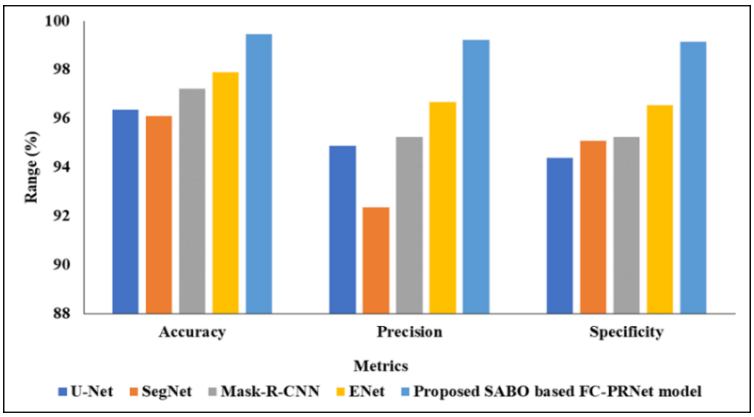

Figure 3: Segmentation validation using accuracy, precision and recall

This suggests the Proposed SABO-based FC-PRNet model is effective for semantic image segmentation, making it a compelling choice for applications that demand high precision and accuracy.

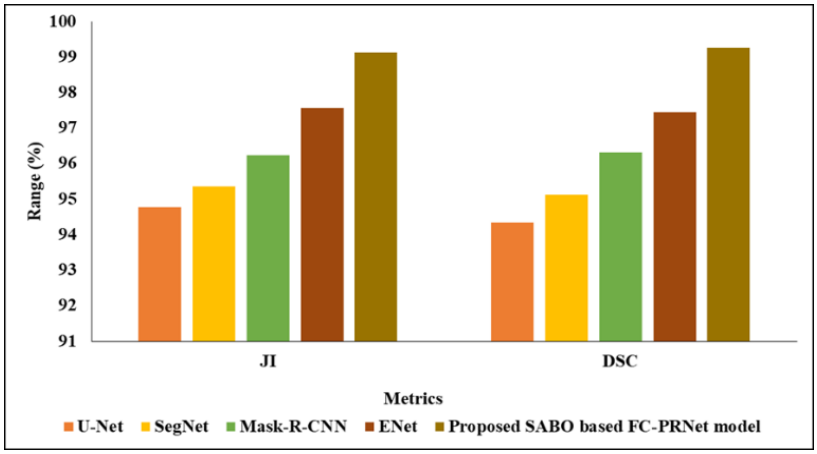

Figure 4: Segmentation validation of the proposed SABO-FC-PRNet segmentation model

4.4. Classification Analysis

Tables 4 and 5 present the training and testing analyses of the SC classification evaluation for the ECA-Net-based VGG16 model.

Table 4: Training phase validation of the proposed ECA-Net-based VGG16 model

Models	Accuracy	Precision	Recall	Specificity	F1-score
AlexNet	82.97	77.39	80.07	87.23	89.32
ResNet	89.06	85.78	87.39	81.32	83.46
InceptionNet	86.86	84.79	86.77	80.09	87.39
VGG16	84.49	79.77	82.05	79.85	81.42
Proposed ECA-Net based on the VGG16 model	93.28	94.33	94.28	94.84	93.25

A comparative evaluation of five image classification models was conducted during the training phase, as shown in Table 4 and Figures 5 and 6, assessing their performance across various metrics. AlexNet achieved 82.97% accuracy, with precision, recall, specificity, and F1-score of 77.39%, 80.07%, 87.23%, and 89.32%, respectively. ResNet achieved improved overall performance, with an accuracy of 89.06%, along with precision, recall, specificity, and F1-score values of 85.78%, 87.39%, 81.32%, and 83.46%, respectively. InceptionNet showcased competitive results, with an accuracy of 86.86% and precision, recall, specificity, and F1-score values of 84.79%, 86.77%, 80.09%, and 87.39%, respectively. VGG16 demonstrated solid performance, with an accuracy of 84.49% and precision, recall, specificity, and F1-score values of 79.77%, 82.05%, 79.85%, and 81.42%, respectively. Notably, the Proposed ECA-Net based on the VGG16 model outperformed all other models, achieving an accuracy of 93.28%.

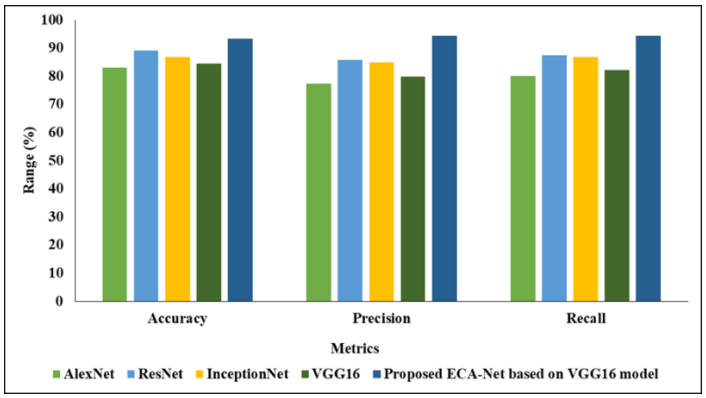

Figure 5: Classification validation on the training phase

The precision, recall, specificity, and F1-score values for this proposed model were notably high at 94.33%, 94.28%, 94.84%, and 93.25%, respectively. These findings demonstrate the efficacy of the proposed ECA-Net in improving classification performance, making it a compelling choice for image recognition tasks requiring high precision and accuracy.

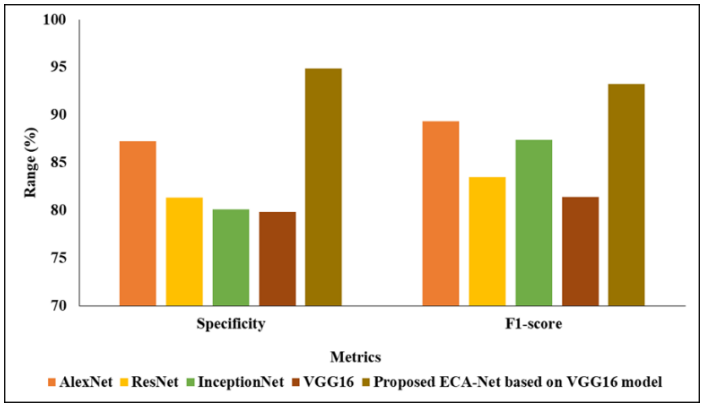

Figure 6: Training phase classification analysis of the ECA-Net-VGG16 model

In a comprehensive evaluation of image classification models, five distinct architectures were assessed using the performance metrics reported in Table 5 and Figures 7 and 8. AlexNet achieved a commendable accuracy of 96.71%, along with high precision, recall, specificity, and F1-score values of 96.92%, 96.82%, 96.33%, and 96.32%, respectively.

Table 5: Testing phase analysis of the proposed ECA-Net-based VGG16 model

Models	Accuracy	Precision	Recall	Specificity	F1-score
AlexNet	96.71	96.92	96.82	96.33	96.32
ResNet	96.82	97.24	97.11	96.42	96.46
InceptionNet	97.55	97.81	97.74	97.45	97.39
VGG16	97.84	98.13	98.03	97.64	97.42
Proposed ECA-Net based on the VGG16 model	99.66	99.35	99.36	99.41	99.25

ResNet showcased comparable results, with an accuracy of 96.82% and precision, recall, specificity, and F1-score values of 97.24%, 97.11%, 96.42%, and 96.46%, respectively. InceptionNet achieved superior performance, with an accuracy of 97.55% and precision, recall, specificity, and F1-score values of 97.81%, 97.74%, 97.45%, and 97.39%, respectively. VGG16 demonstrated strong classification capabilities, achieving 97.84% accuracy, along with precision, recall, specificity, and F1-score values of 98.13%, 98.03%, 97.64%, and 97.42%, respectively. Notably, the Proposed ECA-Net based on the VGG16 model outperformed all other architectures, reaching an impressive accuracy of 99.66%.

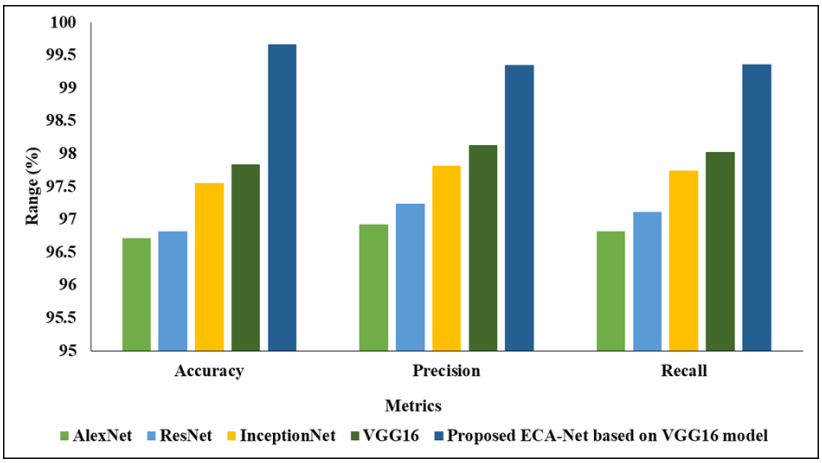

Figure 7: Testing phase analysis of the ECA-Net-VGG16 model

The precision, recall, specificity, and F1-score values for this proposed model were exceptionally high at 99.35%, 99.36%, 99.41%, and 99.25%, respectively. These findings underscore the efficacy of the proposed ECA-Net for achieving state-of-the-art performance in image classification, making it a compelling choice for applications requiring high precision and accuracy.

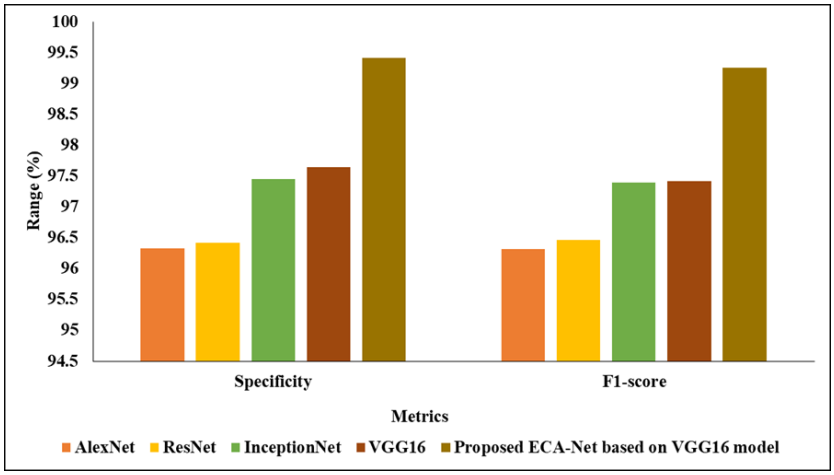

Figure 8: Classification analysis of the testing phase

5. Conclusion

In conclusion, in response to the urgent need for more accurate and effective diagnostic tools in the face of the rising incidence of SC, this study represents an important advance in skin cancer detection, enhancing detection across multiple categories by addressing the limitations of current diagnostic methods. The comprehensive pipeline introduces new techniques to improve the development of preprocessing and classification steps. The use of histogram equalisation as a preprocessing step is an important basis, improving image quality and providing a clear basis for subsequent analysis. Using a fully variable pyramid network for segmentation (FC-PRNet) further refines the system, significantly improves field detection accuracy, and improves Patient outcomes. A major innovation is the inclusion of a subtraction-average-based optimiser (SABO) for hyperparameter tuning during partitioning. These enhancements not only simplify the training process but also enhance the model's robustness by ensuring it is adaptable to diverse data types and potential clinical scenarios. Interactions among these techniques lead to a comprehensive approach to diagnosing multiple categories of SC. The introduction of the Efficient Channel Attention (ECA)-Infused Visual Geometry Group (VGG16) framework, named EC-Net-VGG16, represents a significant improvement in classification by integrating cognitive techniques. The model focuses on relevant factors to improve the accuracy. Achieving exceptional results, the SABO-based FC-PRNet segmentation model exhibits an outstanding 99.45% accuracy, along with 99.12% Jaccard Index (JI) and 99.25% Dice Similarity Coefficient (DSC). Furthermore, the proposed ECA-Net, a classification model based on VGG16, surpasses the existing models with a remarkable 99.66% accuracy and a comparably higher precision of 99.35%. The emphasis on identifying multiple classes underscores the approach's versatility and its ability to address the challenges inherent to various SCs. Future work includes refining hyperparameter tuning in segmentation, exploring new conceptual approaches, and validating robustness on different data types.

Acknowledgement: The authors gratefully acknowledge the support and collaboration of New Horizon College of Engineering, Karunya Institute of Technology and Science, Saranathan College of Engineering, Trichy Research Labs, Quest Technologies, and IPS Health.

Data Availability Statement: The datasets generated and analysed during this study are available from the corresponding author upon reasonable request.

Funding Statement: This research was conducted without external funding from any agencies, organisations, or institutions.

Conflicts of Interest Statement: The authors declare that they have no known financial or personal conflicts of interest that could have influenced the outcomes of this study.

Ethics and Consent Statement: All authors have provided their full consent for this work to be published and made accessible for academic, educational, and research purposes.

References

1. J. Daghrir, L. Tlig, M. Bouchouicha, and M. Sayadi, "Melanoma skin cancer detection using deep learning and classical machine learning techniques: A hybrid approach," *2020 5th International Conference on Advanced Technologies for Signal and Image Processing (ATSIP)*, Sousse, Tunisia, 2020.
2. M. Dildar, S. Akram, M. Irfan, H. U. Khan, M. Ramzan, A. R. Mahmood, S. A. Alsaiari, A. H. M. Saeed, M. O. Alraddadi, and M. H. Mahnashi, "Skin cancer detection: a review using deep learning techniques," *Int. J. Environ. Res. Public Health*, vol. 18, no. 10, p. 5479, 2021.
3. M. Nawaz, Z. Mehmood, T. Nazir, R. A. Naqvi, A. Rehman, M. Iqbal, and T. Saba, "Skin cancer detection from dermoscopic images using deep learning and fuzzy k-means clustering," *Microsc. Res. Tech.*, vol. 85, no. 1, pp. 339–351, 2022.
4. M. Vidya and M. V. Karki, "Skin Cancer Detection using Machine Learning Techniques," *IEEE International Conference on Electronics, Computing and Communication Technologies (CONECCT)*, Bengaluru, India, 2020.
5. M. K. Monika, N. A. Vignesh, C. U. Kumari, M. N. V. S. S. Kumar, and E. L. Lydia, "Skin cancer detection and classification using machine learning," *Mater. Today: Proc*., vol. 33, no. 1, pp. 4266–4270, 2020.
6. A. Murugan, S. A. H. Nair, A. A. P. Preethi, and K. S. Kumar, "Diagnosis of skin cancer using machine learning techniques," *Microprocess. Microsyst*., vol. 81, no. 3, p. 103727, 2021.
7. S. Jinnai, N. Yamazaki, Y. Hirano, Y. Sugawara, Y. Ohe, and R. Hamamoto, "The development of a skin cancer classification system for pigmented skin lesions using deep learning," *Biomolecules*, vol. 10, no. 8, p. 1123, 2020.
8. M. S. Ali, M. S. Miah, J. Haque, M. M. Rahman, and M. K. Islam, "An enhanced technique of skin cancer classification using deep convolutional neural network with transfer learning models," *Mach. Learn. Appl.*, vol. 5, no. 9, p. 100036, 2021.

9. S. S. Chaturvedi, J. V. Tembhurne, and T. Diwan, “A multi-class skin cancer classification using deep convolutional neural networks,” *Multimedia Tools Appl.*, vol. 79, no. 39, pp. 28477–28498, 2020.
10. M. A. Khan, M. Sharif, T. Akram, R. Damaševičius, and R. Maskeliūnas, “Skin lesion segmentation and multiclass classification using deep learning features and improved moth flame optimization,” *Diagnostics*, vol. 11, no. 5, p. 811, 2021.
11. S. M. Thomas, J. G. Lefevre, G. Baxter, and N. A. Hamilton, “Interpretable deep learning systems for multi-class segmentation and classification of non-melanoma skin cancer,” *Med. Image Anal.*, vol. 68, no. 2, p. 101915, 2021.
12. I. Iqbal, M. Younus, K. Walayat, M. U. Kakar, and J. Ma, “Automated multi-class classification of skin lesions through deep convolutional neural network with dermoscopic images,” *Comput. Med. Imag. Graph.*, vol. 88, no. 3, p. 101843, 2021.
13. A. G. Pacheco and R. A. Krohling, “The impact of patient clinical information on automated skin cancer detection,” *Comput. Biol. Med.*, vol. 116, no. 1, p. 103545, 2020.
14. J. Höhn, A. Hekler, E. Krieghoff-Henning, J. N. Kather, J. S. Utikal, F. Meier, F. F. Gellrich, A. Hauschild, L. French, J. G. Schlager, K. Ghoreschi, T. Wilhelm, H. Kutzner, M. Heppt, S. Haferkamp, W. Sondermann, D. Schadendorf, B. Schilling, R. C. Maron, M. Schmitt, T. Jutzi, S. Fröhling, D. B. Lipka, and T. J. Brinker, “Integrating patient data into skin cancer classification using convolutional neural networks: systematic review,” *J. Med. Internet Res.*, vol. 23, no. 7, p. e20708, 2021.
15. M. Kumar, M. Alshehri, R. AlGhamdi, P. Sharma, and V. Deep, “A DE-ANN inspired skin cancer detection approach using fuzzy c-means clustering,” *Mobile Netw. Appl.*, vol. 25, no. 4, pp. 1319–1329, 2020.
16. S. M. Thomas, J. G. Lefevre, G. Baxter, and N. A. Hamilton, “Interpretable deep learning systems for multi-class segmentation and classification of non-melanoma skin cancer,” *Med. Image Anal.*, vol. 68, no. 2, p. 101915, 2021.
17. C. T. Tchapga, T. A. Mih, A. T. Kouanou, T. F. Fonzin, P. K. Fogang, B. A. Mezatio, and D. Tchiotsop, “Biomedical image classification in a big data architecture using machine learning algorithms,” *J. Healthc. Eng.*, vol. 2021, no. 1, p. 9998819, 2021.
18. X. Cao, J. Yao, Z. Xu, and D. Meng, “Hyperspectral image classification with convolutional neural network and active learning,” *IEEE Trans. Geosci. Remote Sens.*, vol. 58, no. 7, pp. 4604–4616, 2020.
19. R. Kaur, R. Kumar, and M. Gupta, “Deep neural network for food image classification and nutrient identification: A systematic review,” *Rev. Endocr. Metab. Disord.*, vol. 24, no. 4, pp. 633-653, 2023.
20. M. Abdar, M. Samami, S. D. Mahmoodabad, T. Doan, B. Mazoure, R. Hashemifesharaki, L. Liu, A. Khosravi, U. R. Acharya, V. Makarenkov, and S. Nahavandi, “Uncertainty quantification in skin cancer classification using three-way decision-based Bayesian deep learning,” *Comput. Biol. Med.*, vol. 135, no. 8, p. 104418, 2021.
21. L. Zhang, J. Zhang, W. Gao, F. Bai, N. Li, and N. Ghadimi, “A deep learning outline aimed at prompt skin cancer detection utilizing gated recurrent unit networks and improved orca predation algorithm,” *Biomed. Signal Process. Control*, vol. 90, no. 4, p. 105858, 2024.
22. M. A. Hussien and A. H. H. Alasadi, “Classification of melanoma skin cancer using deep learning approach,” *TELKOMNIKA*, vol. 22, no. 1, pp. 129–137, 2024.
23. M. M. Hossain, M. M. Hossain, M. B. Arefin, F. Akhtar, and J. Blake, “Combining state-of-the-art pre-trained deep learning models: A noble approach for skin cancer detection using max voting ensemble,” *Diagnostics*, vol. 14, no. 1, p. 89, 2024.
24. H. Haggerty and R. Chandra, “Self-supervised learning for skin cancer diagnosis with limited training data,” *arXiv:2401.00692*, 2024. Available: https://arxiv.org/abs/2401.00692 [Accessed by 01/06/2024].
25. R. Sonia, J. Joseph, D. Kalaiyarasi, N. Kalyani, A. S. A. L. G. G. Gupta, G. Ramkumar, H. S. Almoallim, S. A. Alharbi, and S. S. Raghavan, “Segmenting and classifying skin lesions using a fruit fly optimization algorithm with a machine learning framework,” *Automatika*, vol. 65, no. 1, pp. 217–231, 2024.
26. P. Natha and P. R. Rajeswari, “Advancing skin cancer prediction: A deep dive into hybrid PCA-autoencoder,” *Int. J. Intell. Syst. Appl. Eng.*, vol. 12, no. S8, pp. 442–449, 2024.
27. D. Chanda, M. S. H. Onim, H. Nyeem, T. B. Ovi, and S. S. Naba, “DCENSnet: A new deep convolutional ensemble network for skin cancer classification,” *Biomed. Signal Process. Control*, vol. 89, no. 8, p. 105757, 2024.
28. M. Heenaye-Mamode Khan, N. Gooda Sahib-Kaudeer, M. Dayalen, F. Mahomedaly, G. R. Sinha, K. K. Nagwanshi, and A. Taylor, “Multi-class skin problem classification using deep generative adversarial network (DGAN),” *Comput. Intell. Neurosci.*, vol. 2022, no. 1, p. 1797471, 2022.
29. R. Rajeswari, K. Kalaiselvi, N. Jayashri, P. Lakshmi, and A. Muthusamy, “Meta-heuristic based melanoma skin disease detection and classification using Wolf Antlion Neural Network (WALNN) model,” *Int. J. Intell. Syst. Appl. Eng.*, vol. 12, no. 9s, pp. 87–95, 2024.
30. F. Li, Z. Long, P. He, P. Feng, X. Guo, and X. Ren, “Fully convolutional pyramidal networks for semantic segmentation,” *IEEE Access*, vol. 8, no. 12, pp. 229132–229140, 2020.
31. P. Trojovský and M. Dehghani, “Subtraction-average-based optimizer: A new swarm-inspired metaheuristic algorithm for solving optimization problems,” *Biomimetics*, vol. 8, no. 2, p. 149, 2023.

32. M. Z. Ullah, Y. Zheng, J. Song, S. Aslam, C. Xu, G. D. Kiazolu, and L. Wang, “An attention-based convolutional neural network for acute lymphoblastic leukemia classification,” *Appl. Sci.*, vol. 11, no. 22, p. 10662, 2021.
33. T. M. Aruna, P. Kumar, N. N. Srinidhi, G. N. Divyaraj, S. Asha, A. Thirumalraj, and E. Naresh, “Effective utilisation of geospatial data for peer-to-peer communication among autonomous vehicles using optimized machine learning algorithm,” *Research Article*, 2023. Available: file:///C:/Users/Moham/Downloads/Effective_Utilisation_of_Geospatial_Data_for_peer-.pdf [Accessed by 10/06/2024].
34. UML, “University of Michigan Library Database,” 2023. Available: https://apps.lib.umich.edu/database/link/11961 [Accessed by 10/06/2024].